

A LOG-GAUSSIAN COX PROCESS WITH SEQUENTIAL MONTE CARLO FOR LINE NARROWING IN SPECTROSCOPY

TEEMU HÄRKÖNEN*, EMMA HANNULA

School of Engineering Science
LUT University
Yliopistonkatu 34, FI-53850 Lappeenranta, Finland

MATTHEW T. MOORES

National Institute for Applied Statistics Research Australia
University of Wollongong
Wollongong NSW 2522, Australia

ERIK M. VARTIAINEN, LASSI ROININEN

School of Engineering Science
LUT University
Yliopistonkatu 34, FI-53850 Lappeenranta, Finland

(Communicated by the associate editor name)

ABSTRACT. We propose a statistical model for narrowing line shapes in spectroscopy that are well approximated as linear combinations of Lorentzian or Voigt functions. We introduce a log-Gaussian Cox process to represent the peak locations thereby providing uncertainty quantification for the line narrowing. Bayesian formulation of the method allows for robust and explicit inclusion of prior information as probability distributions for parameters of the model. Estimation of the signal and its parameters is performed using a sequential Monte Carlo algorithm allowing for parallelization of model likelihood computation. The method is validated using simulated spectra and applied to an experimental Raman spectrum obtained from a protein droplet measurement.

1. Introduction. Line narrowing of spectral line shapes is a mathematical procedure that is used to improve the resolution of spectroscopy. The principal aim of line narrowing is to reduce overlap of the line shapes and to infer more accurate information on the line shape position. There is a long history of research in various approaches for line narrowing based on ideas such as Fourier self-deconvolution [11, 13, 14], Tikhonov regularization [4, 17], maximum entropy [1, 18], and Bayesian inference [8, 9, 21]. Nevertheless, the applicability of these algorithms tends to be limited by requirements on input parameters not known in general, meaning that they must be hand-tuned, and also by the signal-to-noise ratio of the measurements.

To consider a specific example, Line-shape Optimized Maximum Entropy linear Prediction (LOMEP) works well only for spectra with a limited number of spectral lines, which all have the same *a priori* known line shape [11]. Nevertheless,

2020 *Mathematics Subject Classification.* Primary: 62F15, 62L12; Secondary: 78M31.

Key words and phrases. Bayesian inference, Fourier self-deconvolution, particle filtering and smoothing, Poisson process, peak detection, statistical signal processing.

* Corresponding author: Teemu Härkönen.

the fundamental idea behind LOMEP is very appealing. It uses a technique called Fourier self-deconvolution [13, 14], where the Fourier transform of the data is divided by the Fourier transform of a parameterized kernel function, resulting in a signal with narrower line shapes. This requires *a priori* knowledge of the line-shape function in the original spectrum. A low-pass filter is applied to the obtained non-decaying signal to ensure high signal-to-noise ratio. After this, a maximum-entropy, linear-prediction algorithm is used to predict the non-decaying signal to yield new narrower line shapes while preserving their respective amplitudes.

The LOMEP algorithm is known to suffer from peak splitting, where individual peaks in the underlying signal are split into two or more peaks, thereby overestimating the number of peaks that are present [12]. The key contribution of this paper is the introduction of a Log-Gaussian Cox Process (LGCP) [20] for this specific application, as a statistical model for the peak locations. An LGCP is a doubly-stochastic process, whose output is defined as a Poisson process and whose intensity function is modelled as a log-Gaussian process. This enables modelling of observed point data that exhibit clustering, the intensity of which can vary spatially or temporally. The LGCP has previously been applied to statistical modelling of disease incidence data [6], wildfire occurrences [23], and crime incidence [24]. Here, the intensity function of the LGCP can be considered to provide automatic smoothing where the parameters of the smoothing kernel are inferred statistically.

In our previous work [10], we incorporated LOMEP as a pre-processing step for empirical Bayesian inference on the line shape parameters using a Sequential Monte Carlo (SMC) algorithm [5]. Here, we extend this approach to a fully-Bayesian statistical model that is capable of providing posterior distributions for the estimated line-narrowed spectrum, along with posterior distributions for the line width and impulse-response length. We sample these model parameters and realizations using SMC, which utilizes a collection of particles to approximate the probability distributions of interest. Our SMC algorithm provides a scalable and parallelizable method of statistical inference for spectroscopic data. In addition to the primary interest of line narrowing, the posterior distributions for the line widths and peak locations have immediate applications in being incorporated as prior distributions for further statistical spectrum analysis techniques [10, 19].

The remainder of this paper is structured as follows. In Section 2, we present our Bayesian statistical model for spectral measurements. In Section 3, this is followed by a description of the SMC algorithm. In Section 4, we formulate our log-Gaussian Cox process model to better estimate the underlying line-narrowed spectrum. In Section 5, prior distributions and other modelling choices are detailed. In Section 6, we present experimental results for our synthetic and real spectroscopic data sets. Finally, in Section 7, we discuss our conclusions and consider future directions for research.

2. Statistical line narrowing model. We observe spectral measurements consisting of N line shapes with additive errors

$$y_k := y(\nu_k) = f(\nu_k; \delta_N(\nu_k), \boldsymbol{\theta}) + \epsilon_k, \quad (1)$$

where $y_k \in \mathbb{R}$ denotes a discretized measurement at a wavenumber location $\nu_k \in \{\nu_1, \dots, \nu_K\}$ with sampling resolution $h > 0$ where $h = |\nu_{k+1} - \nu_k|$. The continuous spectrum model is $f(\nu; \delta_N(\nu), \boldsymbol{\theta})$ with $\delta_N(\nu)$ being a linear combination of N Dirac delta functions and $\boldsymbol{\theta} = (\theta_1, \dots, \theta_P)^T$ being a vector of line shape parameters. The

Gaussian measurement error is $\epsilon_k \sim \mathcal{N}(0, \sigma_\epsilon^2)$ with variance assumed known and zero mean. We denote the vector of all measurements as $\mathbf{y} := (y_1, \dots, y_K)^T$.

The spectrum $f(\nu; \delta_N(\nu), \boldsymbol{\theta})$ is modelled as

$$f(\nu; \delta_N(\nu), \boldsymbol{\theta}) = \sum_{n=1}^N a_n \mathcal{K}(\nu - \nu_n; \boldsymbol{\theta}) = \mathcal{K}(\nu; \boldsymbol{\theta}) * \sum_{n=1}^N a_n \delta(\nu - \nu_n), \quad (2)$$

where $*$ denotes convolution with respect to ν ; $\mathcal{K}(\nu; \boldsymbol{\theta})$ is the common line shape, or kernel, parameterized according to $\boldsymbol{\theta}$; and $a_n \delta(\nu - \nu_n)$ is a Dirac delta function at location ν_n with amplitude a_n . We consider two common line shapes relevant for spectroscopic applications, the Lorentz line shape

$$\mathcal{K}(\nu; \boldsymbol{\theta}) = L(\nu; \gamma) = \frac{1}{\pi\gamma} \frac{\gamma^2}{\nu^2 + \gamma^2}, \quad (3)$$

and the Voigt line shape

$$\mathcal{K}(\nu; \boldsymbol{\theta}) = V(\nu; \sigma, \gamma) = L(\nu; \gamma) * G(\nu; \sigma) = \frac{1}{\pi\gamma} \frac{\gamma^2}{\nu^2 + \gamma^2} * \frac{1}{\sqrt{2\pi\sigma^2}} \exp\left(-\frac{\nu^2}{2\sigma^2}\right), \quad (4)$$

where γ and σ denote scale parameters of Lorentzian and Gaussian line shapes, respectively. In the Fourier domain, the Dirac delta functions can be represented in terms of the Fourier self-deconvolution signal

$$\begin{aligned} \xi(\omega; \boldsymbol{\theta}) &:= \mathcal{F} \left\{ \sum_{n=1}^N a_n \delta(\nu - \nu_n) + a_n \delta(\nu + \nu_n) \right\} \\ &= \frac{\mathcal{F} \{y(\nu) + y(-\nu)\}}{\mathcal{F} \{\mathcal{K}(\nu, \boldsymbol{\theta})\}} = 2 \sum_{n=1}^N a_n \cos(2\pi\omega\nu_n), \end{aligned} \quad (5)$$

where \mathcal{F} is the Fourier transform and ω denotes the Fourier-transformed variable.

The fact that trigonometric functions can be linearly predicted in the ω -domain is the key property utilized in the LOME algorithm, see for example [14]. This can be used to construct a linearly-predicted approximation for the discretized ω -domain representation which we denote by $\xi_{\text{LP}}(\omega_k; \boldsymbol{\theta}, M)$. The signal $\xi_{\text{LP}}(\omega_k; \boldsymbol{\theta}, M)$ is constructed by first truncating the discrete Fourier self-deconvolution signal to length $2 \leq M \leq K$. The truncated signal is then linearly predicted with an impulse response of length $M - 1$, yielding a linearly predicted signal $\xi_{\text{LP}}(\omega_k; \boldsymbol{\theta}, M)$. Given the above, let $x_{\text{LN}}(\nu_k; \boldsymbol{\theta}, M) = \mathcal{F}^{-1} \{ \xi_{\text{LP}}(\omega_k; \boldsymbol{\theta}, M) \}$ denote the line-narrowed spectrum. For details on linear prediction, see [11, 14].

Under the assumptions given in Equation (1) the exact likelihood of the observed spectrum is

$$\mathcal{L}(\mathbf{y} \mid \mathbf{f}(\boldsymbol{\nu}), \sigma_\epsilon^2) = \prod_{k=1}^K \mathcal{N}(y_k; f(\nu_k; \delta_N(\nu_k), \boldsymbol{\theta}), \sigma_\epsilon^2), \quad (6)$$

where $\mathbf{f}(\boldsymbol{\nu}) = (f(\nu_1), \dots, f(\nu_K))^T$ is the underlying spectral signal evaluated at wavenumbers $\boldsymbol{\nu} = (\nu_1, \dots, \nu_K)^T$. However, in practice this signal is unknown and cannot be directly observed. Instead, we approximate it using

$$f(\nu_k; \delta_N(\nu_k), \boldsymbol{\theta}) \approx g(\nu_k, \boldsymbol{\theta}, M) := \mathcal{F}^{-1} \left\{ \xi_{\text{LP}}(\omega_k; \boldsymbol{\theta}, M) \widehat{\mathcal{K}}(\omega_k; \boldsymbol{\theta}) \right\}, \quad (7)$$

where \mathcal{F}^{-1} denotes the inverse Fourier transform and $\widehat{\mathcal{K}}(\omega_k; \boldsymbol{\theta}) = \mathcal{F} \{ \mathcal{K}(\nu_k, \boldsymbol{\theta}) \}$.

For brevity, henceforth we use a shorthand notation for the line-narrowed spectrum $\mathbf{x}_{\text{LN}} := (x_{\text{LN}}(\nu_1; \boldsymbol{\theta}, M), \dots, x_{\text{LN}}(\nu_K; \boldsymbol{\theta}, M))^T$. The likelihood (6) can then be approximated by

$$\mathcal{L}(\mathbf{y} \mid \mathbf{f}(\boldsymbol{\nu}), \sigma_\epsilon^2) \approx \tilde{\mathcal{L}}(\mathbf{y} \mid \mathbf{x}_{\text{LN}}, \sigma_\epsilon^2) = \prod_{k=1}^K \mathcal{N}(y_k; g(\nu_k, \boldsymbol{\theta}, M), \sigma_\epsilon^2). \quad (8)$$

The idea of approximating the likelihood using a Fourier transform is similar in spirit to the Whittle quasi-likelihood [28], but in our case $\tilde{\mathcal{L}}$ also involves linear prediction and deconvolution. Given our quasi-likelihood, the posterior distribution can be formulated as

$$\pi(\mathbf{x}_{\text{LN}}, \boldsymbol{\theta}, M \mid \mathbf{y}, \sigma_\epsilon^2) \propto \tilde{\mathcal{L}}(\mathbf{y} \mid \mathbf{x}_{\text{LN}}, \sigma_\epsilon^2) \pi_0(\mathbf{x}_{\text{LN}} \mid \boldsymbol{\theta}, M) \pi_0(\boldsymbol{\theta}) \pi_0(M), \quad (9)$$

where $\pi_0(\boldsymbol{\theta})$, $\pi_0(M)$, and $\pi_0(\mathbf{x}_{\text{LN}} \mid \boldsymbol{\theta}, M)$ denote prior distributions for the line width, the Fourier self-deconvolution cut-off point, and the line-narrowed spectrum, respectively. The posterior distribution in Equation (9) is not available in closed form and thus we require Bayesian computational methods to obtain stochastic samples from this distribution. The SMC algorithm that we use for this purpose is detailed in the following section.

3. Sequential Monte Carlo. SMC, also known as the particle filter, or sequential importance sampling with resampling, is a class of algorithms for Bayesian computation that are very widely used for statistical signal processing and time series analysis. For a general overview of SMC methods, we recommend [3, 22]. The SMC algorithm that we introduce here employs sequential importance sampling from a series of tempered probability distributions $\pi^{(0)}, \pi^{(1)}, \dots, \pi^{(T)}$ to ultimately obtain samples from the desired posterior distribution defined in Equation (9).

We construct the distribution at step t of the tempering sequence as

$$\pi^{(t)}(\mathbf{x}_{\text{LN}}, \boldsymbol{\theta}, M \mid \mathbf{y}, \sigma_\epsilon^2) \propto \tilde{\mathcal{L}}(\mathbf{y} \mid \mathbf{x}_{\text{LN}}, \sigma_\epsilon^2)^{\kappa^{(t)}} \pi_0(\mathbf{x}_{\text{LN}} \mid \boldsymbol{\theta}, M) \pi_0(\boldsymbol{\theta}) \pi_0(M) \quad (10)$$

where the superscript (t) denotes the iteration of the SMC algorithm and the tempering parameter $\kappa^{(t)}$ is chosen such that $\kappa^{(t-1)} < \kappa^{(t)} < \kappa^{(t+1)} < \dots \leq 1$ with $\kappa^{(0)} = 0$. In Equation (10), the initial state of the particle distribution is equal to the joint prior for $\boldsymbol{\theta}$, M , and \mathbf{x}_{LN} : that is $\pi^{(0)} = \pi_0(\mathbf{x}_{\text{LN}} \mid \boldsymbol{\theta}, M) \pi_0(\boldsymbol{\theta}) \pi_0(M)$. At each subsequent iteration, the particles are updated so that the intermediate tempering distribution approaches the targeted posterior given in Equation (9).

We determine the tempering schedule adaptively, as in [10, 19], such that the relative decrease in effective sample size (ESS), defined as

$$J_{\text{ESS}}^{(t)} = \frac{1}{\sum_{j=1}^J (w_j^{(t)})^2}, \quad (11)$$

is approximately some predefined learning rate η between SMC iterations. Here, $w_j^{(t)}$ is the importance sampling weight for the j th particle $(\mathbf{x}_{\text{LN},j}, \boldsymbol{\theta}_j, M_j)$, where $j = 1, \dots, J$. The incremental unnormalized weights in the SMC algorithm are

$$W_j^{(t)} \propto \frac{\tilde{\mathcal{L}}(\mathbf{y} \mid \mathbf{x}_{\text{LN}}, \sigma_\epsilon^2)^{\kappa^{(t)}}}{\tilde{\mathcal{L}}(\mathbf{y} \mid \mathbf{x}_{\text{LN}}, \sigma_\epsilon^2)^{\kappa^{(t-1)}}} w_j^{(t-1)}, \quad (12)$$

with the normalized weights given by $w_j^{(t)} = W_j^{(t)} / \sum_{j=1}^J W_j^{(t)}$.

As the number of iterations increases, the weights will gradually become concentrated on a small number of particles, hence $J_{\text{ESS}}^{(t)}$ decreases. This can eventually result in a single particle dominating the inference. To avoid this tendency, we employ two additional steps: resampling and mutation of the particles. Resampling is initiated when the ESS drops below a set threshold J_{min} . Each particle is resampled with replacement, using probabilities equal to $w_j^{(t)}$. This often means that particles with the most weight are sampled multiple times, creating duplicates. After resampling, the weights are all reset to $w_j^{(t)} = \frac{1}{J}$. Markov chain Monte Carlo (MCMC) is then used to update the particles to move duplicate particles to different states. The target distribution for the MCMC is defined by the tempered posterior distribution at iteration t as given in Equation (10). We present pseudo-code for our SMC sampled line narrowing method in Algorithm 1.

Algorithm 1 Sequential Monte Carlo sampled line narrowing.

Initialize:

Set $t = 0$ and $\kappa^{(t)} = 0$.

Sample J particles independently from the prior $\pi_0(\boldsymbol{\theta})\pi_0(M)$.

Compute a line-narrowed spectrum $\boldsymbol{x}_{\text{LN},j}$ for each particle $(\boldsymbol{\theta}_j, M_j)$.

Compute the quasi-likelihood $\tilde{\mathcal{L}}(\mathbf{y} \mid \boldsymbol{x}_{\text{LN},j}, \sigma_\epsilon^2)$ for each particle.

Set particle weights $w_j^{(t)} = \frac{1}{J}$.

while $\kappa^{(t)} < 1$ **do**

$t = t + 1$.

Determine $\kappa^{(t)}$ according to the learning rate η .

Update particle weights $w_j^{(t)}$ according to Equation (12).

Compute the effective sample size $J_{\text{ESS}}^{(t)}$ using Equation (11).

if $J_{\text{ESS}}^{(t)} < J_{\text{min}}$ **then**

Resample particles according to their weights.

Set particle weights $w_j^{(t)} = \frac{1}{J}$.

end if

Update particles with MCMC targeting the tempered posterior given by (10).

end while

After the final iteration is complete and $\kappa^{(T)} = 1$, the distribution of the J particles represent samples from the target posterior distribution, Equation (9). However, the marginal posterior $\pi(\boldsymbol{x}_{\text{LN}} \mid \mathbf{y})$ for the line-narrowed spectrum is lacking in physical interpretability. This is due to the phenomenon of “peak splitting,” where individual peaks in the true spectrum $\boldsymbol{f}(\boldsymbol{\nu})$ are split into two or more peaks in the line-narrowed spectrum $\boldsymbol{x}_{\text{LN}}$ [12]. The line-narrowed spectra are approximations of Dirac delta functions, so their marginalization is difficult to visualize accurately. Individual samples from $\pi(\boldsymbol{x}_{\text{LN}} \mid \mathbf{y})$ are illustrated in Figure 1 and we show a simplified illustration of the marginalized posterior for $\boldsymbol{x}_{\text{LN}}$ in Figure 2. This leads us to consider “smoothing” the peaks, or more accurately, estimating the underlying distribution of peak locations ν_n , which we assume to be distributed according to a log-Gaussian Cox process.

4. Log-Gaussian Cox Process. A point process is a countable collection of random locations $\{\nu_1, \nu_2, \dots\}$ within some space, \mathcal{S} . In our case, we take \mathcal{S} to be the space of wavenumbers \mathbb{R}_+ , or more specifically the continuous interval bounding

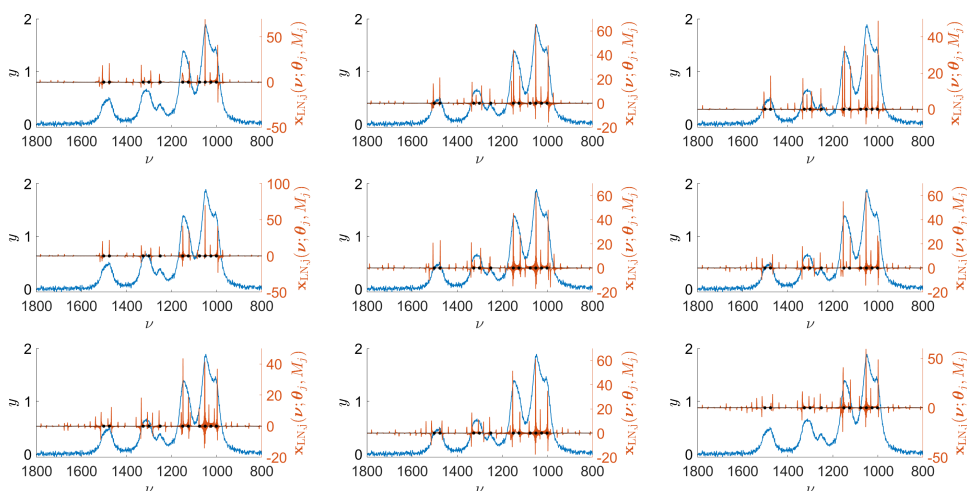


FIGURE 1. Individual samples obtained from the sequential Monte Carlo algorithm for the line narrowing $\mathbf{x}_{\text{LN},j}(\nu; \theta_j, M_j)$ shown in red, overlaid on top of the synthetic spectrum \mathbf{y} , shown in blue.

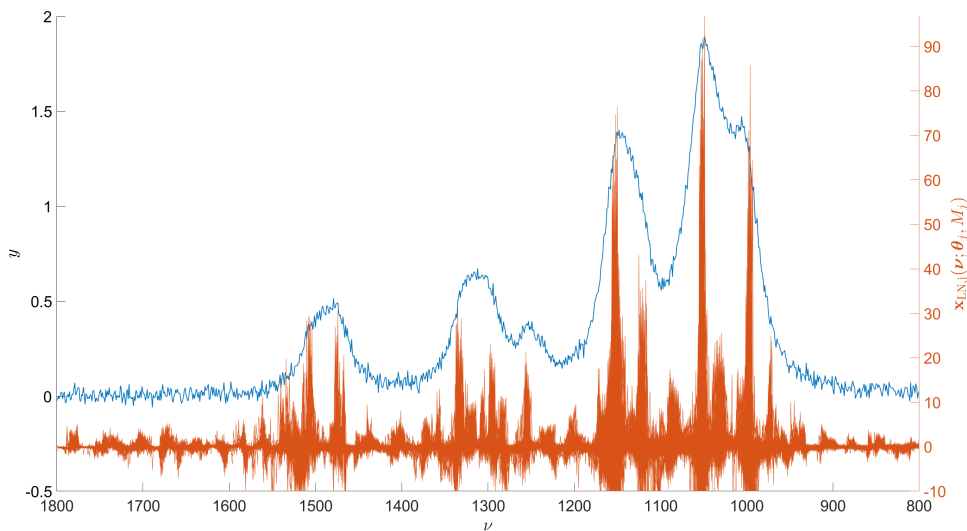


FIGURE 2. In red, a summary of the distribution of posterior samples from $\pi(\mathbf{x}_{\text{LN}} | \mathbf{y})$ for the synthetic spectrum \mathbf{y} , shown in blue. The approximate number, locations, and sizes of the peaks can be inferred from this distribution, but not robustly.

the fingerprint region for organic molecules, $\nu_n \in [800, 1800]$. Closely related to this random set of points is the counting process $\varphi(A)$ for measurable subsets $A \subseteq \mathcal{S}$. For example, if $B = [800, 900]$ and there are two peaks with locations $\nu_1 = 810$ and $\nu_2 = 850$, then $\varphi(B) = 2$.

A Poisson process is a type of point process that satisfies the following properties [15]:

- (i) Whenever $A_1, A_2, \dots, A_Q \subset \mathcal{S}$ are disjoint, then $\varphi(A_1), \varphi(A_2), \dots, \varphi(A_Q)$ are independent random variables. That is,

$$\mathbb{P}\left(\bigcap_{i \in \mathcal{I}} \{\varphi(A_i) = z_i\}\right) = \prod_{i \in \mathcal{I}} \mathbb{P}(\varphi(A_i) = z_i), \quad z_i \in \mathbb{N} \cup \{0\}, \mathcal{I} \subseteq \{1, \dots, Q\}. \quad (13)$$

- (ii) The random variable $\varphi(A)$ follows a Poisson distribution, with expectation

$$\mathbb{E}[\varphi(A)] = \Lambda(A),$$

where $\Lambda(A)$ is known as the intensity measure. Let λ be the Radon-Nikodým derivative of Λ , so that $\Lambda(A) = \int_A \lambda(a) da$, then λ is known as the intensity function.

A log-Gaussian Cox process (LGCP) is a *doubly*-stochastic point process, where the intensity function λ of an inhomogeneous Poisson process is modelled as a stochastic process, or a random function, in itself. Specifically, the logarithm of the intensity is considered to follow a Gaussian process (GP) [20],

$$\log \lambda(\nu) \sim \text{GP}(\mathbf{0}, \Sigma(\nu, \nu'; \boldsymbol{\psi})), \quad (14)$$

where $\Sigma(\nu, \nu'; \boldsymbol{\psi})$ is the covariance function of the GP with parameter vector $\boldsymbol{\psi}$, evaluated at locations $\nu, \nu' \in \mathcal{S}$. We use a squared exponential covariance,

$$\Sigma(\nu, \nu'; \boldsymbol{\psi}) = \sigma_\lambda^2 \exp\left(-\frac{1}{2} \frac{(\nu - \nu')^2}{\ell^2}\right), \quad (15)$$

where σ_λ is the standard deviation of the GP and ℓ is its length scale parameter, so that $\boldsymbol{\psi} = (\sigma_\lambda, \ell)^T$.

The exact likelihood of the LGCP is intractable for continuous \mathcal{S} , so we follow the advice of [20] and discretize the domain. In our case, \mathcal{S} is already partitioned into disjoint subsets A_1, \dots, A_K at equally-spaced locations ν_1, \dots, ν_K , each being h wavenumbers apart, so that $\bigsqcup_{k=1}^K A_k = \mathcal{S}$ and $|\mathcal{S}| = Kh$. In order to fit the LGCP, we need to translate the SMC samples for the line-narrowed spectrum $\mathbf{x}_{\text{LN},j}$ into approximate counts z_k of the number of Dirac delta functions located inside each subset A_k . However, these samples can have negative values due to the Gibbs phenomenon or ringing caused by the approximation of delta functions via Fourier transforms, as can be seen in Figure 2. Thus, we discretize and translate the samples so that a LGCP can be utilized. We initially marginalize the samples with respect to $\boldsymbol{\theta}$ and M as

$$\bar{x}_k := \mathbb{E}_{\boldsymbol{\theta}, M} [x_{\text{LN}}(\nu_k) \mid \mathbf{y}] \approx \frac{y_{\text{area}}}{J} \sum_{j=1}^J \frac{x_{\text{LN},j}(\nu_k; \boldsymbol{\theta}_j, M_j) \mathbb{1}_{x \geq 0}}{\sum_{k=1}^K x_{\text{LN},j}(\nu_k; \boldsymbol{\theta}_j, M_j) \mathbb{1}_{x \geq 0}}, \quad (16)$$

where \bar{x}_k denotes the posterior expectation for the line-narrowed spectrum at ν_k , $y_{\text{area}} = \sum_{k=1}^K y_k$ the area under the measurements, and $\mathbb{1}_{x \geq 0}$ is an indicator function such that

$$\mathbb{1}_{x \geq 0} = \begin{cases} 1, & x_{\text{LN},j}(\nu_k; \boldsymbol{\theta}_j, M_j) \geq 0, \\ 0, & x_{\text{LN},j}(\nu_k; \boldsymbol{\theta}_j, M_j) < 0. \end{cases} \quad (17)$$

Next, we scale the values by a pre-defined constant of proportionality C and round the values to the closest integers. Given this, we obtain discretized and positive values $\mathbf{z} = (z_1, \dots, z_K)^T$ constructed as

$$z_k = \left\lfloor C \bar{x}_k + \frac{1}{2} \right\rfloor \quad (18)$$

where $\lfloor x \rfloor$ denotes the greatest integer $\leq x$.

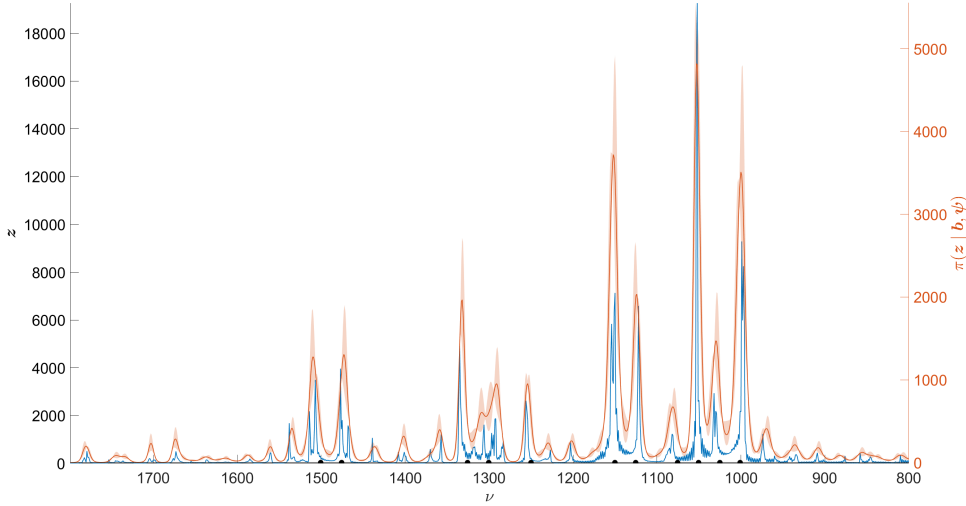


FIGURE 3. The scaled, marginalized, line-narrowed spectrum \mathbf{z} (in blue) and the estimated MAP solution for the LGCP posterior $\pi(\mathbf{b} | \mathbf{z})$ (in red). The shaded area illustrates 90% posterior credible intervals for the LGCP estimate. The true peak locations are shown by 11 black dots.

Given the above, we are able to approximate the likelihood of the LGCP by

$$\mathcal{L}(\mathbf{z} | \mathbf{b}) = \prod_{k=1}^K \frac{\lambda(\nu_k)^{z_k}}{z_k!} \exp\{\lambda(\nu_k)\}, \quad (19)$$

where $\mathbf{b} = (\log \lambda(\nu_1), \dots, \log \lambda(\nu_K))^T$. In turn, the GP prior for \mathbf{b} can be evaluated as

$$\pi_0(\mathbf{b} | \boldsymbol{\psi}) = \frac{1}{\sqrt{(2\pi)^K}} |\Sigma(\boldsymbol{\nu}, \boldsymbol{\nu}; \boldsymbol{\psi})|^{-1/2} \exp\left\{-\frac{1}{2} \mathbf{b}^T \Sigma(\boldsymbol{\nu}, \boldsymbol{\nu}; \boldsymbol{\psi})^{-1} \mathbf{b}\right\}, \quad (20)$$

where $|\Sigma(\boldsymbol{\nu}, \boldsymbol{\nu}; \boldsymbol{\psi})|$ denotes the determinant of the $K \times K$ covariance matrix. The joint posterior distribution is then

$$\pi(\mathbf{b}, \boldsymbol{\psi} | \mathbf{z}) \propto \mathcal{L}(\mathbf{z} | \mathbf{b}) \pi_0(\mathbf{b} | \boldsymbol{\psi}) \pi_0(\boldsymbol{\psi}), \quad (21)$$

where $\pi_0(\boldsymbol{\psi})$ are priors for the parameters of the GP. For inference of the posterior defined in (21), we use maximum *a posteriori* (MAP) estimation via quasi-Newton optimization. Specifically, the limited-memory Broyden–Fletcher–Goldfarb–Shanno (L-BFGS) algorithm [16] as implemented in the GPstuff toolbox [26]. The discretized and positive values \mathbf{z} and corresponding MAP estimate for \mathbf{b} , along with 90% posterior credible intervals, are illustrated in Figure 3.

5. Prior Distributions and Computational Details. We use a continuous uniform distribution for the line width parameter γ for both Lorentz and Voigt profiles, with σ modelled as a truncated normal distribution conditional on γ . A discrete uniform distribution is used for the cut-off parameter M . The priors for the GP covariance parameters $\boldsymbol{\psi}$ are specified on a logarithmic scale. We use Student’s t distributions $t(\mu, \delta^2, \nu_{\text{Fr}})$ parameterized according to mean, variance, and degrees of freedom. We detail these prior distributions in Table 1.

TABLE 1. Prior distributions for the Lorentz and Voigt line shape parameters θ , the Fourier self-deconvolution cut-off parameter M , and the GP covariance parameters ψ .

Prior	Lorentz	Voigt
$\pi_0(\gamma)$	$\mathcal{U}(1, 30)$	$\mathcal{U}(1, 30)$
$\pi_0(\sigma \mid \gamma)$	NA	$\mathcal{N}_+(0.5 \times \gamma, (0.05 \times \gamma)^2)$
$\pi_0(M)$	$\mathcal{U}(10, 80)$	$\mathcal{U}(10, 80)$
$\pi_0(\log\{\sigma_\lambda\})$	$t(0, 100^2, 10)$	$t(0.01, 100^2, 10)$
$\pi_0(\log\{\ell\})$	$t(0.01, 100^2, 10)$	$t(0.01, 100^2, 10)$

More specifically we set $\pi_0(\gamma) = \mathcal{U}(1, 30)$ and $\pi_0(M) = \mathcal{U}(10, 80)$, meaning that the half-width at half-maximum (HWHM) of the peaks is limited to a range between 1 cm^{-1} and 30 cm^{-1} and the number of Fourier self-deconvolution points is limited to lay in in the interval $[10, 80]$. This prior on M has an important effect in regularizing the discrete Fourier approximation given by Equation (7). If M is too large, then the posterior for \mathbf{x}_{LN} will be dominated by ringing artifacts and boundary effects, making it impossible to determine the peak locations. The theoretical maximum number of peaks that can be represented by $g(\nu_k, \theta, M)$ is $0.5M$ [14]. In practice, we recommend setting the upper bound for $\pi_0(M)$ to be at least four times the maximum number of peaks in the spectrum, but small enough that the effect of ringing artifacts is minimized.

The SMC was run with $J = 1000$ particles with residual resampling initiated when ESS falls below a threshold of $J_{\min} = J/2$. We use a Metropolis-Hastings random walk kernel for the MCMC updates. The MCMC proposals for new particles $(\gamma, M)_{1:J}^*$ are constructed as

$$\begin{aligned} (\theta_j^*, \widetilde{M}_j^*) &= (\theta_j, M_j) + \zeta, \\ M_j^* &= \left\lfloor \widetilde{M} + \frac{1}{2} \right\rfloor + \zeta_M, \end{aligned} \tag{22}$$

where $\zeta \sim \mathcal{N}(0, c\Sigma_{\theta, N})$ with $\Sigma_{\theta, N}$ denoting an empirical covariance of the current particles $(\theta, N)_{1:J}$, scaled according to $c \in R_+$ such that the acceptance rate is approximately a pre-defined target acceptance rate, and with a discrete random walk $\zeta_M \sim \mathcal{U}(-1, 1)$. New particles $\mathbf{x}_{LP, j}(\nu, \theta_j^*, M_j^*)$ are then computed according to the linear prediction method. The target acceptance rate was set to 0.30 with 5 MCMC updates during each iteration step.

6. Results. We apply our SMC-sampled LOME algorithm to 4 synthetic spectra as well as to an experimental Raman spectrum. The four cases of synthetic spectra are as follows: first, a spectrum consisting of 10 Lorentzian line shapes with all having the same line width $\gamma = 15$; next, we use a spectrum consisting of 12 Lorentzian line shapes with randomly-sampled line width from a uniform distribution $\mathcal{U}(14, 16)$; in the third and fourth cases, the spectra were generated using 11 Voigt line shapes with identical line shape parameters $\gamma = 15$ and $\sigma = 7.5$; and 11 Voigt line shapes with randomly sampled line shape parameters $\gamma \sim \mathcal{U}(14, 16)$ and $\sigma \sim \gamma + \zeta_\sigma$ where $\zeta_\sigma \sim \mathcal{U}(-1, 1)$. All spectra were constructed using noise variance $\sigma_\epsilon^2 = 0.025^2$.

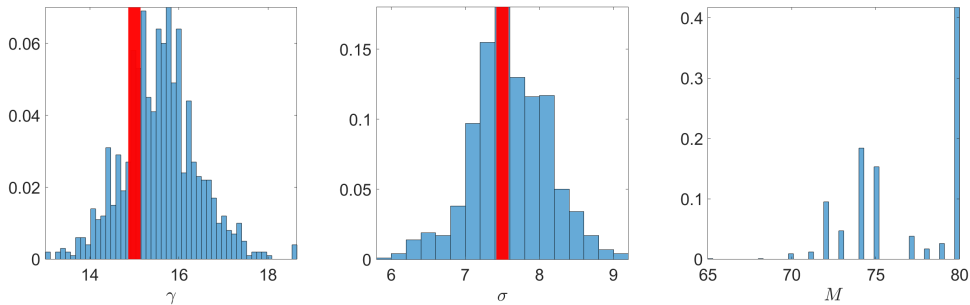


FIGURE 4. Distributions of posterior samples (in blue) for the Voigt line shape parameters γ and σ and the cut-off parameter M , obtained from the sequential Monte Carlo algorithm. The true parameter values are shown by vertical, red bars.

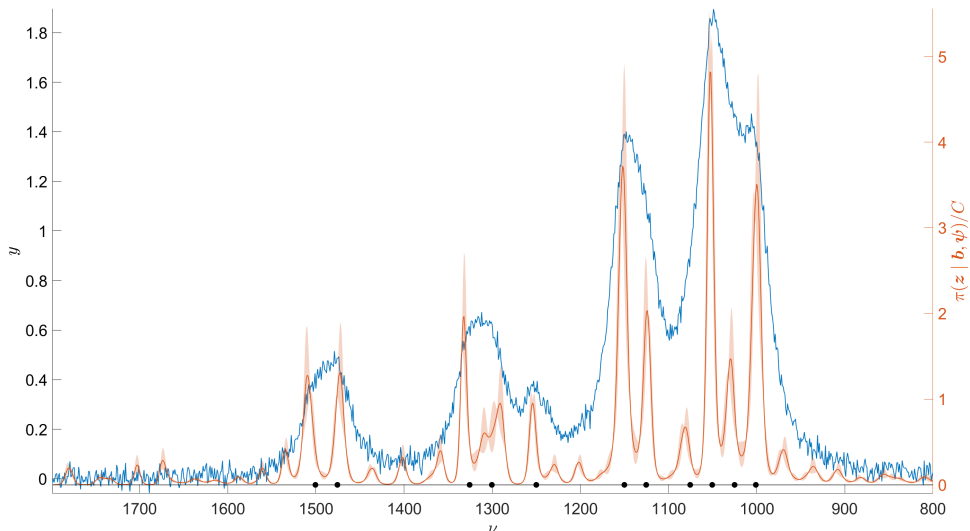


FIGURE 5. The synthetic spectrum (in blue) and the corresponding MAP estimate for the LGCP $\pi(\mathbf{b} \mid \mathbf{z})$ (in red). The shaded area illustrates 90% posterior credible intervals for the LGCP. The true peak locations are shown by 11 black dots.

For the third simulation study (Voigt line shape with fixed γ and σ), individual posterior samples for \mathbf{x}_{LN} are shown in Figure 1, while a summary of the combined posterior $\pi(\mathbf{x}_{LN} \mid \mathbf{y})$ is illustrated in Figure 2. The scaled, marginalized, line-narrowed spectrum \mathbf{z} and the MAP estimate for the LGCP \mathbf{b} are shown in Figure 3. Posterior samples from $\pi(\gamma \mid \mathbf{y})$, $\pi(\sigma \mid \mathbf{y})$, and $\pi(M \mid \mathbf{y})$ are shown in Figure 4. Here, we can see that the true values of $\gamma = 15$ and $\sigma = 7.5$ are contained within the posterior distributions for these parameters. A large amount of posterior mass is concentrated at the maximum value of the Fourier self-deconvolution cut-off parameter, $M = 80$. We tried widening the prior to $\mathcal{U}(10, 120)$, but then the ringing artifacts and boundary effects became amplified beyond what the LGCP smoothing was able to handle. Results with this broader prior are provided in the

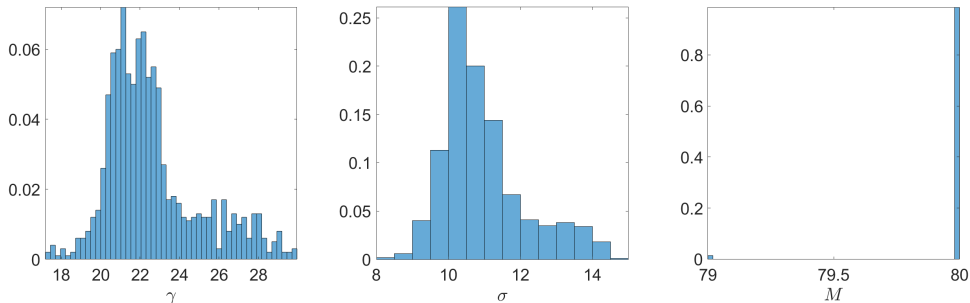


FIGURE 6. Obtained posterior distributions for the Voigt line shape parameters γ and σ and the cut-off parameter M .

online Supplementary Material. We conclude from this that the tuning parameter M is not well-identified by the observed data \mathbf{y} . Rather, the prior on M acts as regularization for the Fourier self-deconvolution.

The MAP estimate for the LGCP, along with 90% posterior credible intervals, are shown in Figure 5 alongside the synthetic Raman spectrum. We can see here that there is a close correspondence between the true peak locations and the local maxima of the LGCP. In comparison with the posterior for \mathbf{x}_{LN} that was shown in Figure 2, the LGCP has made it much easier to identify these peak locations. The results for the remaining three simulation studies were comparable. All of the results for the synthetic data are provided in the online Supplementary Material.

As an application to real-world data, we present an experimental Raman spectrum of a protein droplet sample. This spectrum was measured within the fingerprint region (wavenumbers from 800 to 1800 cm^{-1}) using coherent anti-Stokes Raman microspectroscopy [2]. This region consists of several vibrational bands including Amide I and Amide III bands from 1600 to 1700 cm^{-1} and 1220 to 1250 cm^{-1} , respectively, tyrosine peaks at 830, 850, 1174, 1210, and 1616 cm^{-1} , and a CH_2 peak at 1445 cm^{-1} . The Amide I band is highly congested including six peaks around 1647–1650 cm^{-1} (α -helix peak), 1659–1663 cm^{-1} (random coil peak), 1667–1675 cm^{-1} (β -sheet peak), 1681–1693 cm^{-1} (β -turn peak), 1610–1619 cm^{-1} (Tyr1 peak), and 1590–1609 cm^{-1} (Tyr2 peak).

We use the same prior distributions for this experimental data as for the synthetic spectra, detailed in Table 1. The posterior distributions for the line-shape parameters γ and σ , as well as the cut-off parameter M , are shown in Figure 6. The posterior for M is highly concentrated at the maximum value $M = 80$ with only small probability of $M = 79$. This could be due to the greater number of peaks in the experimental spectrum, shown in Figure 7. Our algorithm found most of the known spectral peak frequencies, even though the measured spectrum is severely corrupted by noise, with average signal-to-noise ratio of approximately 20.

7. Conclusions. We present a Bayesian model for line narrowing of spectroscopic data that is applicable for any parameterizable kernel function. In this paper, we particularly focus on Lorentzian and Voigt line shapes, which are typical of electromagnetic spectra. The key innovation of our method is the use of a log-Gaussian Cox process to provide an interpretable posterior for the line narrowing and correct for unwanted peak splitting effects due to Fourier self-deconvolution.

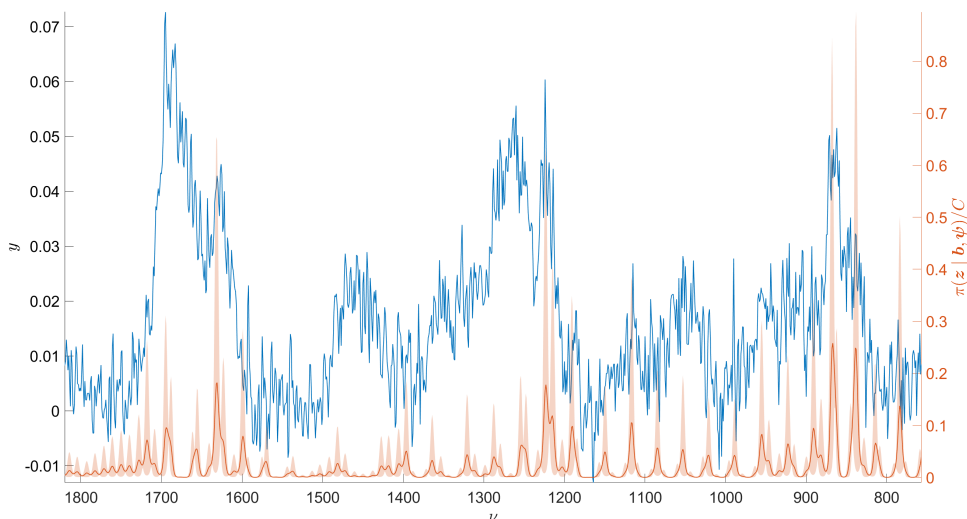


FIGURE 7. The experimental Raman spectrum of a protein droplet sample (in blue) and the corresponding MAP estimate for the LGCP $\pi(\mathbf{b} | \mathbf{z})$ (in red). The shaded area illustrates 90% posterior credible intervals for the LGCP.

This addresses the major limitations of the LOMEP algorithm for line narrowing [11, 12].

In many real-world applications, the true peak locations are unknown *a priori*, which limits the application of existing methods such as [19, 21]. Our proposed method provides posterior distributions for the peak locations, along with the line-shape parameters. These can then be used as input for further chemometric analysis. We have validated our proposed method using synthetic data sets, demonstrating that the smoothed LGCP posterior is able to recover the true peak locations. We also applied our method to an experimental Raman spectrum that exhibited a low signal-to-noise ratio. Nevertheless, we were able to obtain an interpretable posterior for the peak locations that corresponded well with the known spectroscopic properties of that particular protein. This is in contrast to many existing methods, such as [8, 9], that only work well in low-noise environments, or with a small number of peaks.

Although we have focused mainly on Raman spectroscopy here, our method is much more broadly applicable. It has the potential to be used for practically any spectroscopic measurement of electromagnetic phenomena. For example, ionospheric spectra measured by incoherent scatter radar [27], X-ray spectra used for industrial quality control [25], or hyper-spectral radiance measurements in satellite remote sensing [7]. Collection of these types of data is very time-consuming and expensive. Our method could accelerate the process by allowing faster, less-accurate measurements to be made, while using our method as a post-processing step to increase the measurement resolution and to identify regions of interest for further, more accurate measurements.

Acknowledgments. This work has been funded by the Academy of Finland (project numbers 327734, 334816, and 336787).

REFERENCES

- [1] B. Buttingsrud and B. K. Alsberg, A new maximum entropy-based method for deconvolution of spectra with heteroscedastic noise, *Journal of Chemometrics*, **18** (2004), 537–547.
- [2] S. Chatterjee, Y. Kan, M. Brzezinski, K. Koynov, R. M. Regy, A. C. Murthy, K. A. Burke, J. J. Michels, J. Mittal, N. L. Fawzi and S. H. Parekh, Reversible kinetic trapping of fus biomolecular condensates, *Advanced Science*, 2104247.
- [3] N. Chopin and O. Papaspiliopoulos, *An Introduction to Sequential Monte Carlo*, Springer Series in Statistics, Springer, 2020.
- [4] H. Cui, G. Xia, S. Jin, L. Cheng, L. Bai, L. Ma and Y. Fang, Levenberg–Marquardt algorithm with adaptive Tikhonov regularization for bandwidth correction of spectra, *Journal of Modern Optics*, **67** (2020), 661–670.
- [5] P. Del Moral, A. Doucet and A. Jasra, Sequential Monte Carlo samplers, *Journal of the Royal Statistical Society: Series B*, **68** (2006), 411–436.
- [6] P. J. Diggle, P. Moraga, B. Rowlingson and B. M. Taylor, Spatial and spatio-temporal log-Gaussian Cox processes: Extending the geostatistical paradigm, *Statistical Science*, **28** (2013), 542 – 563.
- [7] M. A. Folkman, J. Pearlman, L. B. Liao and P. J. Jarecke, EO-1/Hyperion hyperspectral imager design, development, characterization, and calibration, in *Hyperspectral Remote Sensing of the Land and Atmosphere*, vol. 4151 of Proc. SPIE, 2001, 40–51.
- [8] K. B. Frøhling, T. S. Alstrøm, M. Bache, M. S. Schmidt, M. N. Schmidt, J. Larsen, M. H. Jakobsen and A. Boisen, Surface-enhanced Raman spectroscopic study of DNA and 6-mercaptopto-1-hexanol interactions using large area mapping, *Vibrational Spectroscopy*, **86** (2016), 331–336.
- [9] S. Gulam Razul, W. Fitzgerald and C. Andrieu, Bayesian model selection and parameter estimation of nuclear emission spectra using RJMCMC, *Nuclear Instruments and Methods in Physics Research Section A: Accelerators, Spectrometers, Detectors and Associated Equipment*, **497** (2003), 492–510.
- [10] T. Härkönen, L. Roininen, M. T. Moores and E. M. Vartiainen, Bayesian quantification for coherent anti-Stokes Raman scattering spectroscopy, *The Journal of Physical Chemistry B*, **124** (2020), 7005–7012.
- [11] J. K. Kauppinen, D. J. Moffatt, M. R. Hollberg and H. H. Mantsch, A new line-narrowing procedure based on Fourier self-deconvolution, maximum entropy, and linear prediction, *Applied Spectroscopy*, **45** (1991), 411–416.
- [12] J. K. Kauppinen, D. J. Moffatt and H. H. Mantsch, Nonlinearity of the maximum entropy method in resolution enhancement, *Canadian Journal of Chemistry*, **70** (1992), 2887–2894.
- [13] J. K. Kauppinen, D. J. Moffatt, H. H. Mantsch and D. G. Cameron, Fourier self-deconvolution: A method for resolving intrinsically overlapped bands, *Applied Spectroscopy*, **35** (1981), 271–276.
- [14] J. K. Kauppinen and J. Partanen, *Fourier Transforms in Spectroscopy*, Wiley, Berlin, 2001.
- [15] G. Last and M. D. Penrose, *Lectures on the Poisson Process*, Cambridge University Press, 2017.
- [16] D. C. Liu and J. Nocedal, On the limited memory BFGS method for large scale optimization, *Mathematical Programming*, **45** (1989), 503–528.
- [17] H. Liu, L. Yan, Y. Chang, H. Fang and T. Zhang, Spectral deconvolution and feature extraction with robust adaptive Tikhonov regularization, *IEEE Transactions on Instrumentation and Measurement*, **62** (2013), 315–327.
- [18] V. A. Lórenz-Fonfría and E. Padrós, Maximum entropy deconvolution of infrared spectra: Use of a novel entropy expression without sign restriction, *Applied Spectroscopy*, **59** (2005), 474–486.
- [19] M. T. Moores, K. Gracie, J. Carson, K. Faulds, D. Graham and M. Girolami, Bayesian modelling and quantification of Raman spectroscopy, 2016, arXiv preprint 1604.07299.
- [20] J. Møller, A. R. Syversveen and R. P. Waagepetersen, Log Gaussian Cox processes, *Scandinavian Journal of Statistics*, **25** (1998), 451–482.
- [21] C. Ritter, Statistical analysis of spectra from electron spectroscopy for chemical analysis, *The Statistician*, **43** (1994), 111–127.
- [22] S. Särkkä, *Bayesian Filtering and Smoothing*, Cambridge University Press, 2013.

- [23] L. Serra, M. Saez, J. Mateu, D. Varga, P. Juan, C. Díaz-Ávalos and H. Rue, Spatio-temporal log-Gaussian Cox processes for modelling wildfire occurrence: the case of Catalonia, 1994–2008, *Environmental and Ecological Statistics*, **21** (2014), 531–563.
- [24] S. Shirota and A. E. Gelfand, Space and circular time log Gaussian Cox processes with application to crime event data, *The Annals of Applied Statistics*, **11** (2017), 481 – 503.
- [25] J. Suuronen, M. Emzir, S. Lasanen, S. Särkkä and L. Roininen, Enhancing industrial X-ray tomography by data-centric statistical methods, *Data-Centric Engineering*, **1** (2020), e10.
- [26] J. Vanhatalo, J. Riihimäki, J. Hartikainen, P. Jylänki, V. Tolvanen and A. Vehtari, GP-stuff: Bayesian modeling with Gaussian processes, *Journal of Machine Learning Research*, **14** (2013), 1175–1179.
- [27] I. I. Virtanen, H. W. Tesfaw, L. Roininen, S. Lasanen and A. Aikio, Bayesian filtering in incoherent scatter plasma parameter fits, *Journal of Geophysical Research: Space Physics*, **126** (2021), e2020JA028700.
- [28] P. Whittle, Estimation and information in stationary time series, *Arkiv för Matematik*, **2** (1953), 423–434.

Received xxxx 20xx; revised xxxx 20xx.

E-mail address: teemu.harkonen@lut.fi

E-mail address: emma.hannula@student.lut.fi

E-mail address: mmoores@uow.edu.au

E-mail address: erik.vartiainen@lut.fi

E-mail address: lassi.roininen@lut.fi